INTERSEISMIC DEFORMATION ACROSS THE EASTERN ALTYN TAGH FAULT FROM INSAR MEASUREMENTS

C. J. Liu [1], C. Y. Zhao [2], L. Y. Ji [1], Z. R. Zhang [3], H. Sun [1]

[1] The Second Monitoring and Application Center, China Earthquake Administration, Xi'an, China; liuchuanjinking@163.com (C.L.); dinsar010@hotmail.com (L.J.); sunhele@163.com (H.S.)
[2] School of Geology Engineering and Geomatics, Chang'an University, Xian, China; zhaochaoying@163.com (C.Z.)
[3] School of Resource and Environmental Sciences, Wuhan University, Wuhan, China, zzranature@163.com (Z.Z.)

Commission III, WG III/3

KEY WORDS: InSAR, Altyn Tagh fault, Interseismic deformation, Slip rate

ABSTRACT:

As a new type of earth observation technique, InSAR has a lot of advantages, such as all-weather, all-time, high precision, high density, wide coverage and low cost. It has been widely used in deformation monitoring. Taking the eastern segment of Altyn Tagh fault (ATF) as the object of the research, this paper discussed the application of multi-temporal InSAR technology in the field of interseismic deformation monitoring. We measured the interseismic deformation along the eastern section of ATF using three neighboring descending tracks SAR data from the ERS and Envisat missions. The results show that, first, the validation of InSAR results is better than 2.5 mm/yr, the calibration of InSAR results is about 1.06 mm/yr. Second, the fault slip rate in this segment is about 4~7 mm/yr, and is in the locked condition. Third, The InSAR velocity profile across the fault is the clear asymmetry with respect to ATF, it may be the combined effect of northern (NATF) and southern (SATF) branches of ATF.

1. INTRODUCTION

The ~1800-km-long SW-NE sinistral strike-slip Altyn Tagh fault (ATF), which is the boundary between the northern edge of the Tibetan Plateau and the Tarim basin (Figure 1), has been the focus of an ongoing debate on the role of undeformed blocks (e.g., Avouac and Tapponnier, 1993) and continuum deformation (e.g., England and Molnar, 1997) in Indo-Eruasian collisional models. According to the geomorphological characteristics, ATF is divided into three segments: western segment (between 78-84°E), central segment (between 84-94°E), and eastern segment (between 94-97°E) (Figure 1) (Li, 2001).
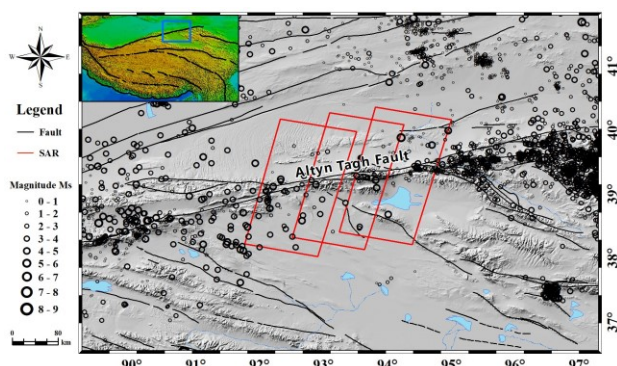

Figure 1. Tectonic setting map of the eastern segment of Altyn Tagh fault. Red box covers the InSAR interferograms, black solid lines shown in active faults, black circles shows precisely located small earthquakes, the inset shows the location of survey region in the Tibetan Plateau.

Due to logistical barriers and inclement weather, it is very hard to carry out field work on ATF. Thus, paleo-earthquakes are not well documented. According to previous studies, there have been 5 large paleo-earthquakes on ATF from Late Pleistocene to Holocene, and the average recurrence period is approximately 800 years. Since 1900, several destructive earthquakes with magnitude 7 or above are known from historical records, including two 1924 Minfeng M 7.3 earthquakes on central segment and the 1932 Changma M 7.6 earthquake on easternmost end. During the last 10 years, Yutian M 7.3 events occurred twice in 2008 and 2012 on southwestern segment of ATF, with the two epicentres 100 km apart.

The slip rate of ATF is an important kinematic description of the Himalayan collision process and a critical constraint for regional seismic hazard estimation. It has been quantified by GPS and InSAR at different segments. Wang and Wright (2012) estimated the left-lateral strike-slip rate of 1±2 mm/yr at 78°E of the western ATF based on ERS-1/2 and Envisat SAR images. At 80°E of ATF, Wright et al. (2004), Wang and Wright (2012) gave a slip rate of 5±5 mm/yr and 2±2 mm/yr, respectively. Elliott et al. (2008) measured the interseismic deformation of ATF at 85°E from ERS-1/2 images for the period of 1993-2000, and the left-lateral strike-slip rate they estimated was 11±5 mm/yr. Zhu et al. (2016) used the same track Envisat data (2003-2010) as Elliott et al. (2008) and their slip rate estimate was 8±0.7 mm/yr. Shen et al. (2001) estimated the slip rate between 85-90°E by using GPS measurements, the results show that the left-lateral rate is 9±2 mm/yr, with a convergence rate of 0±2 mm/yr. At ~86.2°E of ATF, He et al. (2013) estimated a slip rate of 9.0 mm/yr based on a GPS array. For the segment from 89-91°E of ATF, Bendick et al. (2000) reported GPS and levelling data that indicate left-lateral shear rate of 9±5 mm/yr and contraction rate of 3±1 mm/yr, while Wallace et al. (2004) and Zhang et al. (2007) showed a left-lateral slip rate of 9±4 mm/yr and 11.9±3.3 mm/yr respectively. Jolivet et al. (2008) estimated a present-day geodetic slip rate of 8-10 mm/yr across ATF near 94°E using ERS and Envisat radar data covering the

1995-2006 period. Zhang et al. (2007) estimated a slip rate of 8.8±2.3 mm/yr between 93°E and 95°E of ATF using GPS data. At the eastern end of ATF (~96°E), a slip rate of 3.9±2.3 mm/yr was defined based on GPS data (Zhang et al., 2007). Therefore, left-lateral slip on the entire ATF cannot be described by a single slip rate. The slip rate is as low as 2-5 mm/yr at western segment, i.e. 78-80°E. At 85°E and its east, the slip rate decreases gradually from 11 mm/yr to approximately 4 mm/yr at 96°E.

Although GPS and InSAR give slip rates at most segments of ATF, GPS station density is not sufficiently high to determine the pattern of strain accumulation at one kilometer scale, and conventional InSAR measurements are often heavily hampered by atmospheric effects and signal decorrelation. Particularly,

our target segment (between 91.5°E and 95°E) has not been studied using InSAR, and no high spatial resolution measurements are obtained till now. The strike of our target segment being nearly perpendicular to the ERS and Envisat satellites' flying direction and the relatively low vegetation due to arid to semiarid climate make the region ideal for using InSAR to determine interseismic strain accumulation.

This manuscript presents an analysis of 185 SAR images from the C band ERS and Envisat satellites spanning the 1995-2011 period using InSAR technique. These images provide a coverage at high spatial resolution for the eastern segment of ATF and allow us to identify spatial slip deficit rates variations along the fault.

Track	176		405		133	
Satellite	ERS	ENVISAT	ERS	ENVISAT	ERS	ENVISAT
Scenes	24	40	25	24	27	45
Time span (yyyymmdd)	19951118 20110109	20030406 20100926	19951030 20110125	20031014 20100803	19951011 20091008	20030403 20100819

Table 1. SAR data list

2. INSAR DATA PROCESSING STRATEGY

Processed radar data were acquired by the ERS1/2 and Envisat satellites on three contiguous descending tracks (the frames are shown in Figure 1, and the dates are given in Table 1), operating at a wavelength of 56.3 mm. Continuous observations were provided for 16 years from October 1995 to January 2011. Overlapping with each other, the three tracks together cover about 255 km long continuous section of ATF between longitudes 91.5°E and 95.0°E (Figure 1).

The basic InSAR processing techniques employed herein are similar to those of our previous studies (Ji et al., 2013, 2015, 2016). The interferometric processing was performed with GAMMA software (Werner et al., 2000). The two-pass InSAR approach (e.g. Massonnet and Feigl, 1998; Rosen et al., 2000) was utilized to form interferograms. The effects of topography were removed from the interferograms using a filled 1-arc-sec (~30 m) resolution Shuttle Radar Topography Mission (SRTM) digital elevation model (DEM) (Farr and Kobrick, 2000) obtained from NASA's Land Processes Distributed Active Archive Center (LP DAAC, https://e4ftl01.cr.usgs.gov/). In order to improve the signal-to-noise ratio, interferograms were downsampled to 12 looks in range and 60 looks in azimuth (240 m × 240 m) and were filtered using an adaptive filter function based on the local fringe spectrum (Goldstein and Werner 1998), with window dimensions of 64×64 pixels, respectively. This filtering strategy efficiently removes high-frequency noise and renders the phase unwrapping considerably easier.

The main limitation of low-amplitude tectonic signal detection using InSAR is that orbital error and atmospheric delay projected into the line-of-sight direction can be at the same level as tectonic signals, or even larger, reaching tens of centimetres (Zebker et al. 1997). In order to remove residual orbit errors, we applied the following procedure. First, a priori velocity model by the interferometric time spans was established from a screw dislocation model (Savage and Burford, 1973) constrained by the GPS horizontal-component

velocity (Zheng et al., 2017). Second, a residual interferogram was obtained through subtracting the priori velocity model from the original interferogram. Third, a planar trend surface was estimated as orbital error and removed from each residual interferogram. Four, the priori velocity model was added back. Atmospheric errors consist of propagation delay through tropospheric and ionospheric layers. Here we consider only tropospheric noise, because the ionospheric propagation delay is comparatively weak for the ERS1/2 and Envisat C-band data (Gray et al. 2000). European Center for Median-Range Weather Forecast ERA-I (ERA-Interim) atmospheric reanalysis was used to correct atmospheric delay (Jolivet et al., 2011). Specifically, the global ERA-Interim weather model was applied to determine the atmospheric delay close to the time (i.e. within a few hours) of each SAR acquisition. Then, the phase-elevation relation at each grid node of the weather model was estimated and a delay map for each SAR acquisition date was obtained through interpolation in spatial and vertical. At last, the atmospheric-delay-corrected interferogram was achieved through removing the model.

There will be a higher coherence, if interferograms were spanned in a short time interval. However, small tectonic signals, such as signals that across ATF, are more difficult to detect. Therefore, we selected pairs of images based on the following spatial and temporal baselines threshold: (i) 350d < Delta_T < 500d and Bperp < 400 m; (ii) 500d < Delta_T < 1000 and Bperp < 300 m; and (iii) 1000d < Delta_T and Bperp < 200 m. This spatial and temporal baselines selection strategy efficiently minimize geometric decorrelation and errors due to the topography, and maximize the deformation signal in the data. Stacking the interferograms is one efficient way to enhance the tectonic signal (e.g., Zebker et al. 1997; Wright et al. 2001; Biggs et al. 2007; Wang et al., 2009). By averaging many interferograms over the same area, random noise such as atmospheric signals can be subdued, small-scale persistent motion (such as interseismic deformation) can be highlighted, and cumulative trends can be extracted. Stacking N short-baseline and long-timespan interferograms can reduce the

variance of atmospheric errors by a factor of $\sqrt{2}$ (Zebker et al. 1997; Biggs et al. 2007). In this study, we use the π-RATE (Poly-Interferogram Rate And Time-series Estimator) software package developed by Biggs et al. (2007), Elliot et al. (2008)

and Wang et al. (2009, 2012) to calculate the stacked velocity of the northeastern segment of ATF. Pixels that are coherent in five or more of the component interferograms are included in the stack.
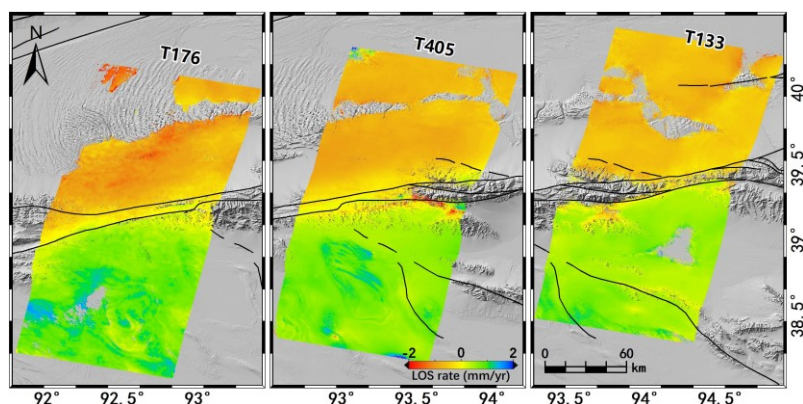

Figure 2. Interseismic deformation field for Eastern Altyn Tagh fault. Rate maps for all three tracks produced with quadratic orbit estimation and with ERA-I atmospheric correction. LOS rate is the rate of ground motion in the satellite line of sight, where a positive value indicates motion toward from the satellite.

3. INSAR VELOCITY FIELD

Here, we use the InSAR technique with Envisat and ERS satellite SAR data acquired on three neighboring descending tracks to map the interseismic strain accumulation velocity along the ~255 km long SW-NE trending section of ATF (between 91.5°E and 95°E) in northeastern Tibetan plateau (Figure 2). As shown in Figure 2, the resulting means that Line-Of-Sight (LOS) InSAR velocity field obtained from π-RARE reveals a clear picture of the interseismic deformation along ATF, with the velocity difference across the fault reaches up to 1 ~ 2 mm/yr. The deformation field shows a gradual change in velocity across the fault. The changing is consistent with the left-lateral sense of motion between the Tibetan plateau and Tarim plate, warm colors are indicated movements away from satellites (i.e., westerly) and cool colors are referred to movements toward (i.e., easterly) satellites which are flying in descending (i.e., heading southward) orbits. The interferograms we use are fairly evenly distributed in time, so the displayed stacks of interferograms is approximate with the average rate over the total time interval of the stacks (Figure 2).

4. EVALUATION OF THE INSAR-DERIVED VELOCITY

4.1 Validation of overlapping regions from adjacent tracks

The trace of ATF clearly defines the boundary between the red and blue areas in Figure 2, which correspond to movement away and toward from the satellite, respectively. The resulting rate maps are shown in Figure 2. In all three rate maps, there is a clear change in LOS velocity across the Eastern ATF that is qualitatively consistent with left-lateral strike-slip interseismic motion, respectively. We also calculate the consistency of adjacent rate in overlapping areas, and then plot histograms of the velocity differences in Figure 3. Assume that the LOS signal is caused by surface motion, the motion is predominantly horizontal and is parallel to the local strike of ATF (N78°E), we converted the mean LOS velocities to fault-parallel (FP) InSAR velocities taking into account the viewing geometry including the local radar look angle (Lyons and Sandwell, 2003).
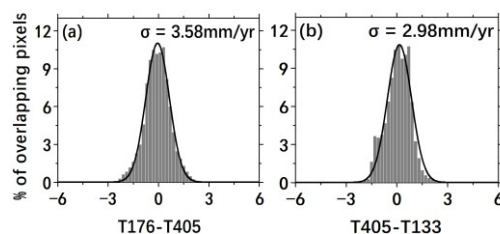

Figure 3. Histograms of the differences between overlapping pairs of rate maps. The black line on each histogram is the best fitting Gaussian, and the number above is the standard deviation of this Gaussian.

The two histograms indicate that the mean values are about zero, the standard deviations of the best fitting Gaussian distribution of 3.58 and 2.98 mm/yr for T176-T405 and T405-T133, respectively. These values can be considered as estimates of $\sqrt{2} \times$ the velocity uncertainties for the individual rate maps, giving 1σ values of 2.5 and 2.1 mm/yr for T176 and T133, respectively. T405 overlaps with both T176 and T133, so we take the mean of the 1σ values for T176 and T133, which is 2.30 mm/yr.

4.2 Comparison with GPS data

The profiles are marked by blue line in Figure 4 (right), the InSAR surface deformation velocities which are measured within ~500 m distance of either side of these profiles are plotted in Figure 4 (left). Topographic elevation along the profiles (shaded areas) is shown in order to reveal any potential correlation between the topography and InSAR measurements, and no correlation is shown between the deformation signal and the local topography. This result suggest that tropospheric effects in the estimated velocity field should be insignificant. Profiles of fault parallel velocities plotted in Figure 4 better illustrate the excellent agreement between the InSAR and GPS measurements. Visual comparison of the InSAR velocity and projected GPS velocities shows a good agreement between these two independent data sets. The difference between the GPS and InSAR velocity has an average of 6.11 mm/yr and a

standard deviation of 1.06 mm/yr. The profiles are consistent overall with a classic arctangent shape predicted by elastic models across a strike-slip fault (Savage and Burford, 1973). It is worth noting that those profiles are satisfactorily flattened at a distance of more than a few tens of kilometers from the fault zone, suggesting that the residual orbital errors can be

negligible. The hypothesis of minimal vertical deformation is justified by the fact that the independent horizontal GPS are in a good agreement with the InSAR measurement: if significant vertical velocity signal was present, disagreement will be found when comparing horizontal GPS displacement only with InSAR data.
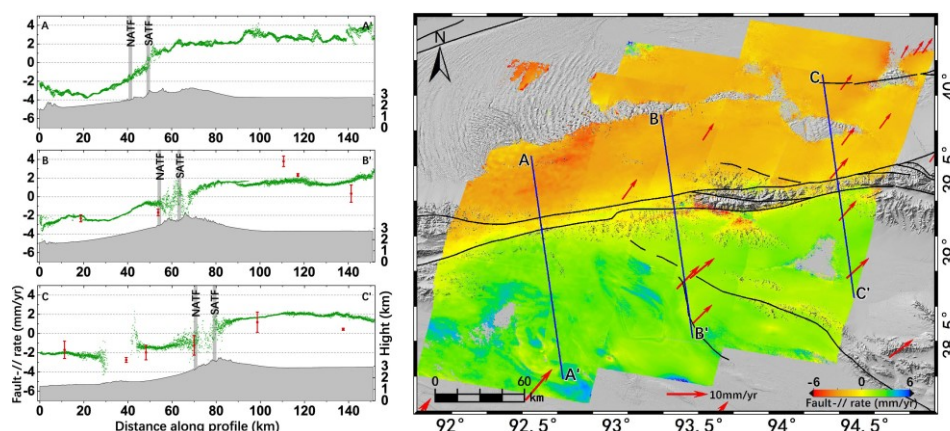

Figure 4. Interseismic deformation profiles across the Eastern Altyn Tagh. Left figure is three cross-fault deformation profiles, InSAR points are shown in green, GPS velocities and 2σ error bars are overlain on the profiles in red. Right figure is InSAR deformation map in fault parallel, black lines shows the location of cross-fault profiles, red arrows represent GPS horizontal velocity.

5. CONCLUSION

We using multi-temporal InSAR technology to monitor the interseismic deformation of eastern Altyn Tagh fault. The results show that the validation of InSAR results is better than 2.5 mm/yr, and the calibration of InSAR results is about 1.06 mm/yr. An obvious slip rate near fault, deformation direction is consistent with the left-lateral strike-slip movement, and this conclusion is consistent with the results of geological survey. The fault slip rate in this segment is about 4~7 mm/yr, and the western segment slip rate is significantly higher than eastern segment in my survey region. The InSAR velocity profile across the fault is obviously asymmetrical to ATF, which may be the comprehensive effect of NATF and SATF.

ACKNOWLEDGEMENTS

REFERENCES

Avouac, J. and Tapponnier, P. 1993. Kinematic model of active deformation in central Asia. Geophysical Research Letters 20(10), pp. 895-898.

Bendick, R., Bilham, R., Freymueller, J., Larson, K., and Yin, G., 2000. Geodetic evidence for a low slip rate in the Altyn Tagh fault system. Nature 404, pp. 69-72.

Biggs, J., Wright, T., Lu, Z., and Parsons, B., 2007. Multi-interferogram method for measuring interseismic deformation: Denali Fault, Alaska. Geophysical Journal International 170(3), pp. 1165-1179.

Elliott, J., Biggs, J., Parsons, B., and Wright, T., 2008. InSAR slip rate determination on the Altyn Tagh Fault, northern Tibet, in the presence of topographically correlated atmospheric delays. Geophysical Research Letters 35(12), pp. L12309.

England, P., and Molnar, P., 1997. Active deformation of Asia: from kinematics to dynamics. Science 278, pp. 647-650.

Farr, T., and Kobrick, M., 2000. Shuttle Radar Topography Mission produces a wealth of data. Eos, Transactions American Geophysical Union 81(48), pp. 583-585.

Goldstein, R., and Werner, C., 1998. Radar interferogram filtering for geophysical applications. Geophysical research letters 25(21), pp. 4035-4038.

Gray, A., Mattar, K., and Sofko, G., 2000. Influence of ionospheric electron density fluctuations on satellite radar interferometry. Geophysical Research Letters 27(10), pp. 1451-1454.

He, J., Vernant, P., Chéry, J., Wang, W., Lu, S., Ku, W., Xia W., and Bilham, R., 2013. Nailing down the slip rate of the Altyn Tagh fault. Geophysical Research Letters 40(20), pp. 5382-5386.

Ji, L., Hu, Y., Wang, Q., Xu, X., and Xu, J., 2015. Large-scale deformation caused by dyke intrusion beneath eastern Hainan Island, China observed using InSAR. Journal of Geodynamics 88, pp. 52-58.

Ji, L., Lu, Z., Dzurisin, D., and Senyukov, S., 2013. Pre-eruption deformation caused by dike intrusion beneath Kizimen volcano, Kamchatka, Russia, observed by InSAR. Journal of Volcanology and Geothermal Research 256, pp. 87-95.

Ji, L., Zhang, Y., Wang, Q., Xin, Y., Li, J., 2016. Detecting land uplift associated with enhanced oil recovery using InSAR

in the Karamay oil field, Xinjiang, China. Int. J. Remote Sens. 37(7), pp. 1527-1540.

Jolivet, R., Grandin, R., Lasserre, C., Doin, M. P., and Peltzer, G., 2011. Systematic InSAR tropospheric phase delay corrections from global meteorological reanalysis data. Geophysical Research Letters, 38(17), pp. 351-365.

Jolivet, R., Cattin, R., Chamot-Rooke, N., Lasserre, C., and Peltzer, G., 2008. Thin-plate modeling of interseismic deformation and asymmetry across the Altyn Tagh fault zone. Geophysical Research Letters 35, pp. L02309.

Li, H., 2001. The formation age of Altyn Tagh fault zone and the contribution of its strike-slipping to the uplifting of north Qinghai-Tibet plateau. PhD thesis. Chinese Academy Geological Sciences, Beijing. (in Chinese).

Lyons, S., and Sandwell D., 2003. Fault creep along the southern San Andreas from interferometric synthetic aperture radar, permanent scatterers, and stacking. Journal of Geophysical Research: Solid Earth 108(B1), pp. 1101-1124.

Massonnet, D., and Feigl, K., 1998. Radar interferometry and its application to changes in the Earth's surface. Reviews of geophysics 36(4), pp. 441-500.

Rosen, P., Hensley, S., Joughin, I., Li, F., Madsen, S., Rodriguez, E., and Goldstein, R., 2000. Synthetic aperture radar interferometry. Proceedings of the IEEE 88(3), pp. 333-382.

Rosen, P., Hensley, S., Zebker, H., Webb, F., and Fielding, E., 1996. Surface deformation and coherence measurements of Kilauea Volcano, Hawaii, from SIR-C radar interferometry. Journal of Geophysical Research: Planets 101(E10), pp. 23109-23125.

Savage, J., and Burford, R., 1973. Geodetic determination of relative plate motion in central California. Journal of Geophysical Research 78(5), pp. 832-845.

Shen, Z., Wang, M., Li, Y., Jackson, D., Yin, A., Dong, D., and Fang, P., 2001. Crustal deformation along the Altyn Tagh fault system, western China, from GPS. Journal of Geophysical Research: Solid Earth 106(B12), pp. 30607-30621.

Wallace, K., Yin, G., and Bilham, R., 2004. Inescapable slow slip on the Altyn Tagh fault. Geophysical Research Letters 31(9), pp. L09613

Wang, H., and Wright, T., 2012. Satellite geodetic imaging reveals internal deformation of western Tibet. Geophysical Research Letters 39(7), pp. L07303.

Wang, H., Wright, T., and Biggs, J., 2009. Interseismic slip rate of the northwestern Xianshuihe fault from InSAR data. Geophysical Research Letters 36(3), pp. L03302.

Wang, H., Wright, T., Yu, Y., Lin, H., Jiang, L., Li, C., and Qiu, G., 2012. InSAR reveals coastal subsidence in the Pearl River Delta, China. Geophysical Journal International 191(3), pp. 1119-1128.

Werner, C., Wegmüller, U., Strozzi, T., and Wiesmann, A., 2000. GAMMA SAR and interferometric processing software. Proceedings of ERS-Envisat Symposium, Gothenburg.

Wright, T., Parsons, B., England, P., and Fielding, E., 2004. InSAR observations of low slip rates on the major faults of western Tibet. Science 305(5681), pp. 236-239.

Wright, T., Parsons, B., and Fielding, E., 2001. Measurement of interseismic strain accumulation across the North Anatolian Fault by satellite radar interferometry. Geophysical Research Letters 28(10), pp. 2117-2120.

Zebker, H., and Goldstein, R., 1986. Topographic mapping from interferometric synthetic aperture radar observations. Journal of Geophysical Research: Solid Earth 91(B5), pp. 4993-4999.

Zebker, H., Rosen, P., and Hensley, S., 1997. Atmospheric effects in interferometric synthetic aperture radar surface deformation and topographic maps. Journal of Geophysical Research: Solid Earth 102(B4), pp. 7547-7563.

Zhang, P., Molnar, P., and Xu, X., 2007. Late Quaternary and present-day rates of slip along the Altyn Tagh Fault, northern margin of the Tibetan Plateau. Tectonics 26(5), pp. TC5010.

Zheng, G., Wang, H., Wright, T., Lou, Y., Zhang, R., Zhang, W., Shi, C., Huang J., and Wei, N., 2017. Crustal Deformation in the India-Eurasia Collision Zone From 25 Years of GPS Measurements. Journal of Geophysical Research: Solid Earth 122(11), pp. 9290-9312.

Zhu, S., Xu, C., Wen, Y., and Liu, Y., 2016. Interseismic deformation of the Altyn Tagh fault determined by Interferometric Synthetic Aperture Radar (InSAR) measurements. Remote Sensing 8(3), pp. 233.